

Direct Observation of a Transiently Formed Isomer During Iodoform Photolysis in Solution by Time-Resolved X-ray Liquidography

Chi Woo Ahn^{a,b}, Hosung Ki^b, Joonghan Kim^c, Jeongho Kim^d, Sungjun Park^{a,b}, Yunbeom Lee^{a,b}, Kyung Hwan Kim^{b,†}, Qingyu Kong^e, Jiwon Moon^c, Martin Nors Pedersen^f, Michael Wulff^f, and Hyotcherl Ihee^{*a,b}

^aDepartment of Chemistry, Korea Advanced Institute of Science and Technology (KAIST), Daejeon 305-701, Republic of Korea

^bCenter for nanomaterials and chemical reactions, Institute for Basic Science (IBS), Daejeon, 34141, Republic of Korea

^cDepartment of Chemistry, The Catholic University of Korea, Bucheon, 14662, Republic of Korea

^dDepartment of Chemistry and Chemical Engineering, Inha University, 100 Inha-ro, Nam-gu, Incheon, 22212, Republic of Korea

^eSoleil synchrotron, Saint-Aubin, 91192, France

^fEuropean Synchrotron Radiation Facility (ESRF), Grenoble Cedex 9, France

[†]Current address: Department of Physics, AlbaNova University Center, Stockholm University, SE-10691 Stockholm, Sweden

Corresponding Author

*E-mail: hyotcherl.ihee@kaist.ac.kr

Table of Contents

Page number

SI Text	3 – 11
Methods and Sample Preparation	3
Density Functional Theory Calculation	4
Molecular Dynamics Simulations	5
Sine-Fourier Transform	5
Global Fit Analysis	6
Scaling of 1.0 mJ/mm² Data to 3.2 mJ/mm² Data	8
Structure Determination of <i>Iso</i>-CHI₂-I	9
Comparison of Structural Optimization of <i>iso</i>-CHI₂-I by Various DFT Methods	10
SI Figures	
Figure S1.	12
Figure S2.	13
Figure S3.	14
Figure S4.	15
SI Tables	
Table S1.	16
Table S2.	17
Table S3.	18
SI References (with full authorship of Gaussian 09 software)	19

SI Text

Methods and Sample Preparation. The time-resolved X-ray liquidography (TRXL) experiment was performed at the ID09 beamline in the European Synchrotron Radiation Facility (ESRF). A pump-probe method using an optical laser pump pulse and a hard X-ray probe pulse was adopted to monitor the progress of the reaction. The detailed TRXL setup is reported in the literature.¹⁻² Four hundred milliliters of a CHI₃ (Sigma-Aldrich, 99.9 %) solution in cyclohexane at 20 mM concentration was used and circulated through a sapphire jet nozzle. A stable 300- μm -thick liquid sheet was produced by the nozzle at a speed ensuring a fresh sample for each pair of laser and X-ray pulses. The solution was replaced every hour to have a fresh aliquot of solution for each measurement. A 200 μJ laser pulse at 267 nm was generated by frequency tripling the 800 nm output from an 1-kHz repetition-rate, amplified Ti:sapphire laser to initiate the photodissociation reaction of CHI₃. To avoid multiphoton excitation, the laser pulse was stretched to 1.2 ps inside the Chirped Pulse Amplifier. The laser beam was subsequently focused to a spot of $240 \times 230 \mu\text{m}^2$ at the sample, and a fluence of $3.2 \text{ mJ}/\text{mm}^2$ was achieved. After the CHI₃ sample was excited by the laser pulse, a time-delayed X-ray pulse was delivered to the sample to probe the progress of the reaction. The quasi-monochromatic ($\Delta E/E \sim 3 \%$) X-ray pulse of 100 ps duration have 5×10^8 photons per pulse, and the center energy of the X-ray pulse was 17.25 keV. With a synchronized mechanical chopper, the X-ray pulse was focused to a spot of $100 \times 60 \mu\text{m}^2$ at the sample. The scattering signals were collected by a CCD detector (Rayonix MX 170, 1920×1920 pixels, 89 μm pixel size) in 2×2 binning mode with a sample-to-detector distance of 36.7 mm and an exposure time of 1 second per image. To probe the CHI₃ photolysis, the scattering signals were collected at various pump-probe delays ($\Delta t = 100 \text{ ps}, 300 \text{ ps}, 1 \text{ ns}, 3 \text{ ns}, 10 \text{ ns}, 30 \text{ ns}, 300 \text{ ns},$ and $1 \mu\text{s}$). The scattering signal at a negative time delay, $S(q, -3 \text{ ns})$, which contains the signal

from an unexcited sample, was subtracted from the signals at other positive time delays to obtain the difference scattering signals, $\Delta S(q,t)$. We found that, due to rapid solvent expansion after 30 ns, the baseline is tilted for the difference scattering curves measured at time delays later than 30 ns. To minimize the baseline problem, the laser fluence was reduced to 1.0 mJ/mm² for the measurements at $\Delta t = 30$ ns, 300 ns, and 1 μ s. The data measured with 1.0 mJ/mm² fluence were scaled to the 3.2 mJ/mm² data by comparing the data measured at common time delays, as will be further discussed later.

Density Functional Theory Calculation. The initial structures of the reactants and candidate intermediates were obtained from density functional theory (DFT) calculations. We used the ω B97X³ functional as the DFT exchange-correlation functional, and all the calculations were done using the Gaussian 09 package.⁴ It is known that the ω B97X functional can accurately predict the C–I distance in halomethanes and haloethanes.⁵ For carbon and hydrogen atoms, aug-cc-pVTZ (AVTZ) all-electron basis sets were used and, to consider the scalar relativistic effects that arise from the iodine atom, dhf-TZVPP small-core relativistic effective core potential (RECP) was used.⁶ Hereafter, this combination is denoted as dhf-TZVPP+AVTZ. For the structure optimization of *iso*-CHI₂–I, we used the broken-symmetry method to include the biradical character of the isomer. Solvent effects (cyclohexane) were implicitly included by applying an integral equation formalism polarizable continuum model (IEFPCM) for all the calculations. The optimized XYZ coordinates of the chemical species involved in the CHI₃ photolysis are summarized in Table S1.

We performed additional DFT calculations to examine the DFT functional dependence on the molecular structures. For these calculations, B3LYP, PBE0, M06-2X, APFD, and MN12-SX were used with the same basis sets and IEFPCM method. In addition, B3LYP/6-311G**, B3LYP/Sadlej pVTZ and ω B97X/6-311G** were performed to examine the basis set dependence.

It is noted that the scalar relativistic effects were not considered in these three calculations (B3LYP/6-311G**, B3LYP/Sadlej pVTZ, and ω B97X/6-311G**). The optimized structural parameters of the chemical species involved in the CHI_3 photolysis are listed in Table S2.

Molecular Dynamics (MD) Simulations. To determine the cage contribution to the $\Delta S(q,t)$, we performed molecular dynamics (MD) simulation for all the chemical species in the reaction. The program MOLDY⁷ was used for running MD simulations, which has successfully simulated the molecules in the solution phase in previous works.⁸⁻⁹ For the simulation, we used one solute molecule embedded in 256 cyclohexane molecules in a cubic box of ~ 26 Å. All simulations were performed at ambient temperature (300 K) with a solvent density of 0.779 g/cm³. The radial distribution functions (RDFs) were calculated from the simulation and further used for calculating the scattering intensity.

Sine-Fourier Transform. The difference RDF, $r^2\Delta S(r)$, where r is the interatomic distance, is a measure of the radial electron density change around an excited atom as a function of r in real space. The difference RDF was obtained by sine-Fourier transform of $q\Delta S(q)$ using the following equation:

$$r^2\Delta S(r) = \frac{r}{2\pi^2} \int_0^\infty q\Delta S(q) \sin(qr) dq \quad (1)$$

To take account of the finite q range of the experimental data, $q\Delta S(q)$ is convoluted with a Gaussian function, $\exp(-q^2\alpha)$, giving the modified $r^2\Delta S(r)$ as follows:

$$r^2\Delta S(r) = \frac{r}{2\pi^2} \int_0^\infty q\Delta S(q) \sin(qr) e^{-q^2\alpha} dq \quad (2)$$

For the damping constant, α , we used a value of 0.03 Å².

Global Fit Analysis. The difference scattering curves, $q\Delta S(q,t)$, were analyzed using our home-made algorithm based on least-square fitting method that minimizes the sum of the reduced chi-square (χ_v^2). χ_v^2 represents the difference between the experimental and theoretical curves as follows:

$$\chi_v^2 = \sum_{j=\text{time delay}} \frac{\chi_j^2}{N - p - 1} \quad (3)$$

$$\chi_j^2 = \sum_i \frac{(S_{\text{theory}}(q_i, t_j) - S_{\text{exp}}(q_i, t_j))^2}{\sigma_{i,j}^2} \quad (4)$$

where N is the total number of data points (for example, if $S(q,t)$ at each time delay has M data points in q space and $S(q,t)$ were measured at L time points, then $N = M \times L$), p is the number of fitting parameters, and $\sigma_{i,j}$ is the standard deviation of data at i -th q point (q_i) and j -th time delay (t_j). Since $q\Delta S(q,t)$ at all positive time delays are connected to reaction kinetics, the fitting was done globally to minimize χ_v^2 . Hence, the global fit parameters contain kinetic parameters such as rate constants for all reaction pathways, branching ratios of the photoproducts, excitation ratio of photoexcited molecules, and structural parameters of solute molecules. The χ_v^2 minimization was done using the MINUIT package provided at CERN.¹⁰ In the global fit analysis, we fit the experimental $q\Delta S(q,t)$ against the theoretical $q\Delta S(q,t)$. The experimental $q\Delta S(q,t)$ was fitted in the q range of 1.0 – 8.0 Å, which has 506 data points. The theoretical $q\Delta S(q,t)$ was modeled by considering three major components, the solute-only term, the solute-solvent cross term (so-called cage term), and the solvent-only term as follows:

$$\begin{aligned}
\Delta S(q,t) &= \Delta S_{solute}(q,t) + \Delta S_{cage}(q,t) + \Delta S_{solvent}(q,t) \\
&= \Delta S_{solute-related}(q,t) + \Delta S_{solvent}(q,t) \\
&= \frac{1}{R} \left[\sum_k c_k(t) S_k(q) - S_g(q) \sum_k c_k(0) \right] \\
&\quad + \left[\left(\frac{\partial S}{\partial T} \right)_\rho \Delta T(t) + \left(\frac{\partial S}{\partial \rho} \right)_T \Delta \rho(t) \right]
\end{aligned} \tag{5}$$

where R is the number ratio of the solvent molecules to solute molecules, k is the index of the solute species (reactants, intermediates, and products), $c_k(t)$ is the fraction of k -th species as a function of time t , $S_k(q)$ is the solute-related (sum of solute-only and cage terms) scattering intensity of k -th species, and $S_g(q)$ is the scattering intensity of reactants ($g = \text{reactants}$). The solvent-only term, $\Delta S_{solvent}(q,t)$, consists of two differentials, $(\partial S(q)/\partial T)_\rho$ and $(\partial S(q)/\partial \rho)_T$. $(\partial S(q)/\partial T)_\rho$ is the change in the scattering intensity with respect to a temperature change at constant density, $(\partial S(q)/\partial \rho)_T$ is the change in the scattering intensity with respect to a density change in the solvent at constant temperature. $\Delta T(t)$ and $\Delta \rho(t)$ are the time-dependent changes in the temperature and density of the solvent, respectively. The solvent differentials, $(\partial S(q)/\partial T)_\rho$ and $(\partial S(q)/\partial \rho)_T$ were determined from a separate measurement on an optical dye in cyclohexane. $\Delta S_{cage}(q)$ was extracted from the atom-atom pair distribution functions, $g(r)$, from MD simulations. We chose the $\omega\text{B97X/dhf-TZVPP+AVTZ}$ method to obtain the initial structure of solute molecules needed to calculate $\Delta S_{solute}(q)$ because the ωB97X functional is known to provide accurate C–I distances in halomethanes and haloethanes.⁵ For the global-fit structural parameters to refine the actual geometry of the solute molecules, we used the C–I bond lengths of CHI_3 and CHI_2 , the I–I bond lengths of I_2 and *iso*- CHI_2 –I, and the C–I–I bond angle of *iso*- CHI_2 –I whereas other structural parameters were fixed at the values provided by the $\omega\text{B97X/dhf-TZVPP+AVTZ}$ method. After structural refinement, $\Delta S(q)$ is no longer "theoretical" $\Delta S(q)$ because the structure of solute molecules are modified from DFT-optimized structure. Thus, to distinguish the structure-refined

$\Delta S(q)$ from the theoretical $\Delta S(q)$, we named the structure-refined $\Delta S(q)$ as "calculated" $\Delta S(q)$. The calculated $q\Delta S(q,t)$ of solute, cage, and solvent terms are shown in Figure S1.

Once the calculated $q\Delta S(q,t)$ curves that best fit the experimental $q\Delta S(q,t)$ curves are obtained, $c_k(t)$ can be extracted with respect to the kinetic model used for constructing calculated $q\Delta S(q,t)$ curves (see Eqn. (5)). For instance, the $c_k(t)$ values of I radicals are obtained by the following procedure. For the solute term, the scattering signal from I radicals appear as atomic scattering intensity, but, in the difference scattering signal $q\Delta S(q,t)$, this contribution actually disappears because the number of I atoms remains constant. Nevertheless, whenever a reaction involving I radicals occurs, the molecular scattering contribution from the counterparts of the I radical in the reaction (for example, for $\text{CHI}_3 \rightarrow \text{CHI}_2 + \text{I}$, the counterparts are CHI_3 and CHI_2) contribute to $q\Delta S(q,t)$ and thus the amount of I radicals is automatically determined through stoichiometry. For the cage term, an MD simulation is run for an I atom embedded in a box of solvent molecules and the RDFs are obtained from the MD trajectories. These RDFs are used to calculate theoretical scattering curves for the cage term of I radicals via Fourier transformation. For the solvent term, the energetics related with I radicals indirectly contribute the changes of temperature and density of the solvent, which constitute the solvent term.

Scaling of 1.0 mJ/mm² Data to 3.2 mJ/mm² Data. When a high fluence (3.2 mJ/mm²) of laser excitation is used, it was found that the amplitude of $q\Delta S(q)$ increases significantly at the time delays later than 30 ns ($\Delta t = 30$ ns, 300 ns, and 1 μ s), especially at low q values ($< 3.5 \text{ \AA}^{-1}$). As a result, the baseline of $q\Delta S(q)$ is tilted for $q\Delta S(q)$ measured at $\Delta t = 30$ ns, 300 ns, and 1 μ s. The anomalous increase of $q\Delta S(q)$ is attributed to rapid vaporization of cyclohexane, which makes the $(\partial S(q)/\partial \rho)_T$ term incompatible with the simple hydrodynamic theory used in our analysis. To minimize the baseline problem at late time delays, it was necessary to reduce the laser fluence to

1.0 mJ/mm². In this study, the data at early time delays ($\Delta t = 100$ ps, 300 ps, 1 ns, 3 ns, and 10 ns) were measured with high laser fluence (3.2 mJ/mm²) and the data at late time delays ($\Delta t = 30$ ns, 300 ns, and 1 μ s) were measured with low laser fluence (1.0 mJ/mm²). When merging the two sets of data measured with the different laser fluences, we checked whether the reaction mechanism is not affected by the laser fluence. To do so, we measured the data at several common time delays (100 ps, 10 ns, and 30 ns) and compared the solute terms of difference scattering curves at those time delays. As shown in Figure S1, the region of $q > 3 \text{ \AA}^{-1}$ is dominated by the solute contribution and therefore we used that region for scaling the low-power data to the high-power data. The best scaling factor for low-power data was calculated to be 2.58 and the scaled results are shown in Figure S2. As shown in Figure S2, the high-power data well matches the scaled low-power data, implying that the reaction mechanism remains the same with the laser excitation of two different laser fluences. Consequently, we scaled the low-power data measured at 30 ns, 300 ns and 1 μ s with the scaling factor of 2.58.

Structure Determination of *iso*-CHI₂-I. Two structural parameters, I2–I3 distance (d_{I-I}) and C–I2–I3 angle (θ_{C-I-I}), were optimized in the global fit analysis to determine the structure of the transiently formed *iso*-CHI₂-I. The fit errors were estimated using the MINUIT software package with the MINOS error estimation method.¹⁰ MINOS estimates the error of each parameter at one standard deviation away from the optimum value, which corresponds to a likelihood distribution of 68.3 %. Figure S3 illustrates the three-dimensional $\Delta\chi^2$ ($\Delta\chi^2 = \chi^2 - \chi^2_{\min}$) surface and its contour plot projected onto a plane of the two structural parameters of *iso*-CHI₂-I, giving the correlations and uncertainties of the two structural parameters at 100 ps. The $\Delta\chi^2$ boundaries of 1, 4, and 9, which correspond to likelihood distributions of 68.3 %, 95.3 %, and 99.7 %, respectively, are shown in the contour plot. Therefore, the limit enclosing the $\Delta\chi^2 = 1$ boundary is used to estimate

the error for each parameter. From the likelihood distribution, the structural parameters at 100 ps were determined to be $d_{I-I} = 2.870 \pm 0.012 \text{ \AA}$ and $\theta_{C-I-I} = 133.6 \pm 2.1^\circ$. To determine d_{I-I} and θ_{C-I-I} more accurately, the structural analysis was extended to the data at other time delays (300 ps – 1 μ s), as listed in Table S3. The weighted average of the two structural parameters determined for all the time delays can be obtained as follows:¹¹

$$\langle x \rangle_w = \frac{\sum_{i=\text{timedelay}} w_i x_i}{\sum_{i=\text{timedelay}} w_i}, \quad w_i = \frac{1}{\sigma_i^2} \quad (6)$$

where $\langle x \rangle_w$ is the weighted average of the structural parameter (d_{I-I} or θ_{C-I-I}), x_i is the optimized structural parameter at the i -th time delay, and σ_i is the standard deviation of the structural parameter at i -th time delay. The average standard deviation for $\langle x \rangle_w$ is given by

$$\sigma_{\text{average}} = \frac{1}{\sqrt{\sum_{i=\text{timedelay}} \sigma_i^{-2}}} \quad (7)$$

The weighted averages and corresponding standard deviations of the structural parameters were determined to be $d_{I-I} = 2.922 \pm 0.004 \text{ \AA}$ and $\theta_{C-I-I} = 133.9 \pm 0.8^\circ$.

Comparison of Structural Optimization of *Iso*-CHI₂-I by Various DFT Methods. Based on the results of various DFT calculations, we systematically compared how the choices of functional and basis set affect the structure of iodine-containing species. As shown in Table S2, structural parameters optimized by B3LYP/dhf-TZVPP+AVTZ are closer to the experimental values than those optimized by B3LYP/6-311G**, indicating that the scalar relativistic effects play a crucial role for the optimization of the molecular structure of iodine-containing species. In addition, optimized structural parameters are significantly affected by the choice of DFT functional (Table

S2). For example, the parameters optimized by ω B97X and MN12-SX are much closer to the experimental ones than those optimized by B3LYP. We note that, although MN12-SX/dhf-TZVPP+AVTZ method, among various DFT methods, gives the optimized structure that are the closest to the experimentally determined structures of *iso*-CHI₂-I, such optimized structure still deviates from the experimental structure, calling for the refinement of DFT-optimized structure. In addition, we found that, regardless of the calculation method, DFT calculation overestimates $d_{\text{I-I}}$ and underestimate $\theta_{\text{C-I-I}}$. This discrepancy between DFT-optimized structures and global-fit structures can be attributed to three factors: (a) spin-orbit coupling (SOC), (b) multireference character of *iso*-CHI₂-I, and (c) implicit solvent model. In this study, SOC and multireference character were not fully taken into account. In addition, the implicit solvent model may not be appropriate for optimizing the structure of *iso*-CHI₂-I because potential energy surface of *iso*-CHI₂-I is broad and shallow¹² compared with CHI₃, implying that the structural parameters of *iso*-CHI₂-I can change significantly depending on the treatment of surrounding solvent molecules. For these reasons, the DFT-optimized structure of *iso*-CHI₂-I varies significantly compared with the structures of other iodine-containing species. Similarly, I-I distance of other *iso*-polyhalomethanes such as *iso*-CH₂I-I was overestimated by DFT calculation (Note that the solvent effect and SOC were not considered.)¹³⁻¹⁴ compared with the experimental value. The I-I distance of *iso*-CH₂I-I in cyclohexane determined by TRXL was reported to be 2.97 Å,¹⁵ which is shorter than DFT-optimized I-I distances (3.019 Å,¹⁴ 3.042 Å,¹³ and 3.073 Å¹³). In this regard, we expect that the predicted values of $d_{\text{I-I}}$ and $\theta_{\text{C-I-I}}$ of *iso*-CHI₂-I can improve by considering SOC, multireference character, and explicit solvent model appropriately.

SI Figures

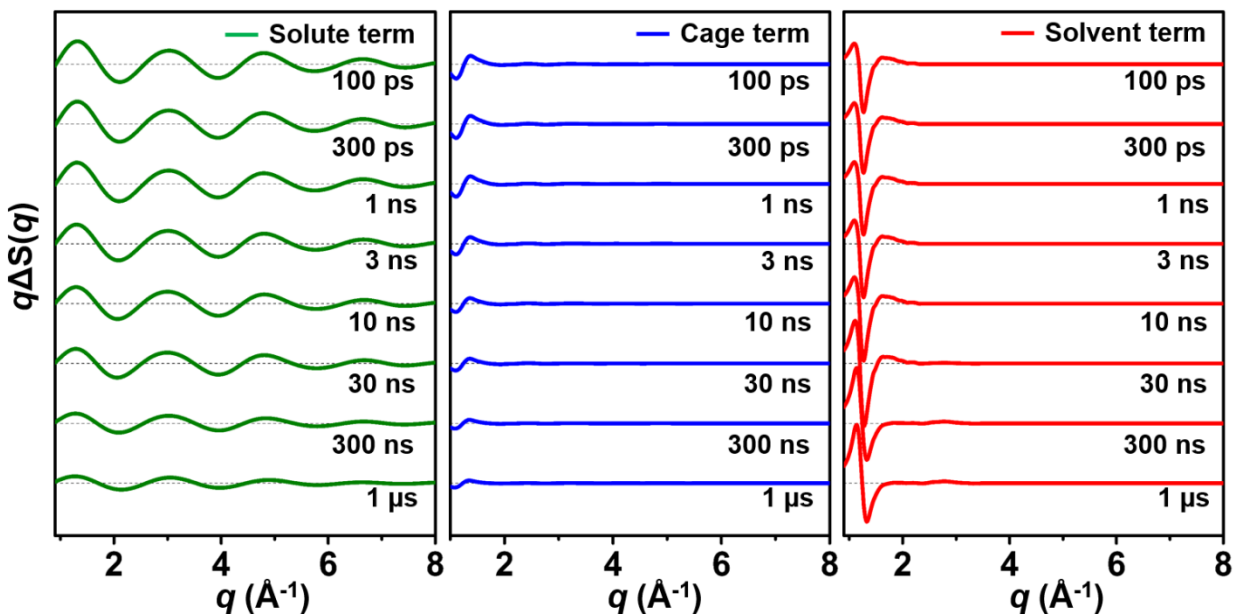


Figure S1. Decomposition of the theoretical $q\Delta S(q,t)$ into three principle contributions as a function of time delay. The $q\Delta S(q,t)$ of solute term (green), cage term (blue), and solvent term (red) from 100 ps to 1 μ s. For better comparison, cage terms were multiplied by a factor of 5 and the solvent terms at 300 ns and 1 μ s were multiplied by a factor of 0.2. All three panels are on the same scale.

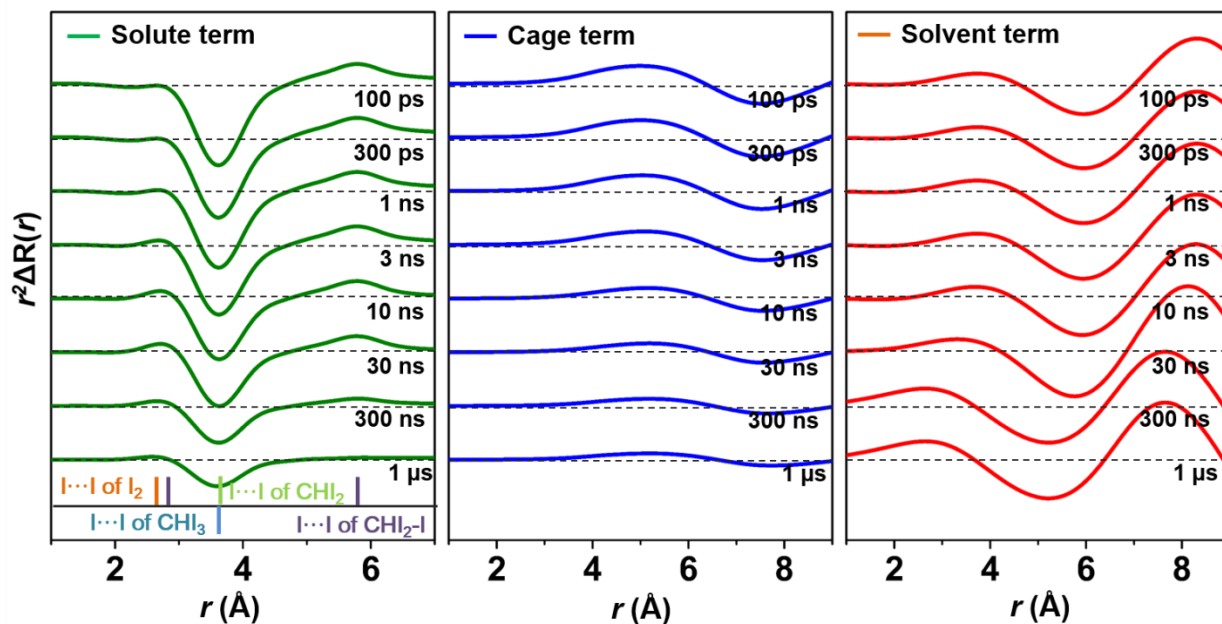


Figure S2. Difference RDFs, $r^2\Delta R(r,t)$, of the solute term (green), cage term (blue), and solvent term (red) from 100 ps to 1 μ s. $r^2\Delta R(r,t)$ were obtained by sine-Fourier transform of $q\Delta S(q,t)$ shown in Figure S1. The solute-related atom-atom distances are displayed at the bottom of the solute terms. For better comparison, cage terms were multiplied by a factor of 5 and the solvent terms at 300 ns and 1 μ s were multiplied by a factor of 0.2. All three panels are on the same scale.

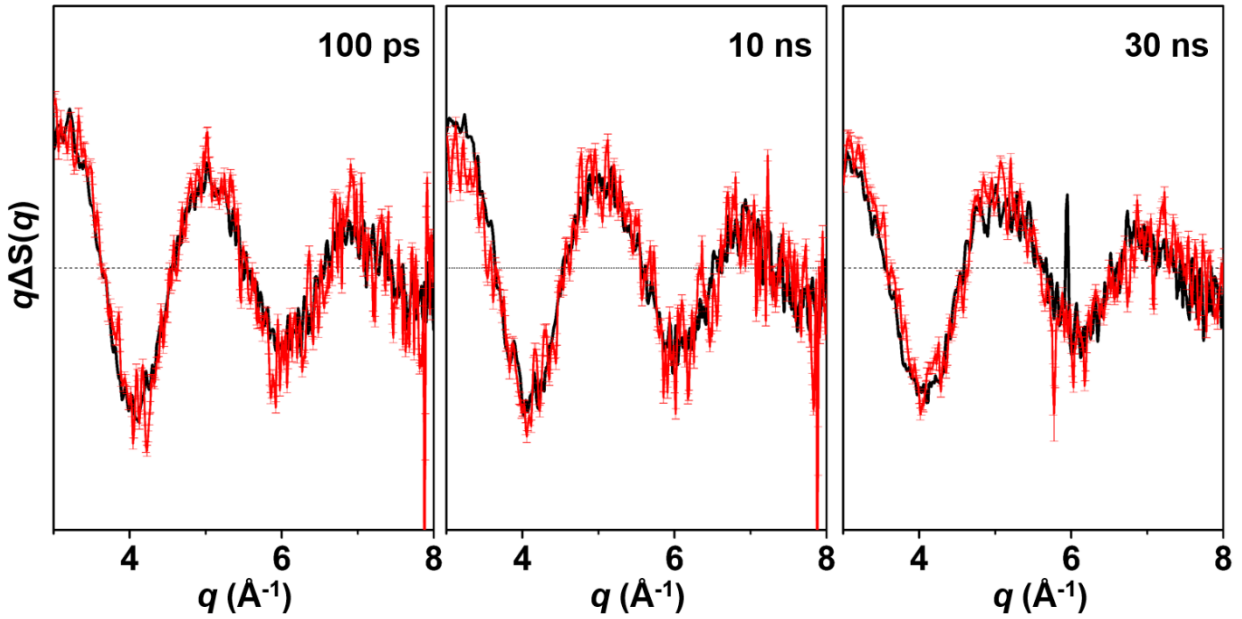


Figure S3. Comparison of $q\Delta S(q,t)$ measured with different laser fluences at common time delays (100 ps, 10 ns, and 30 ns). $q\Delta S(q,t)$ measured with high laser fluence (3.2 mJ/mm^2 , black) and low laser fluence (1.0 mJ/mm^2 , red) are shown. The best scaling factor for the low-power data is 2.58. Note that the high-power data well match the scaled low-power data within the standard deviation. All three panels are on the same scale.

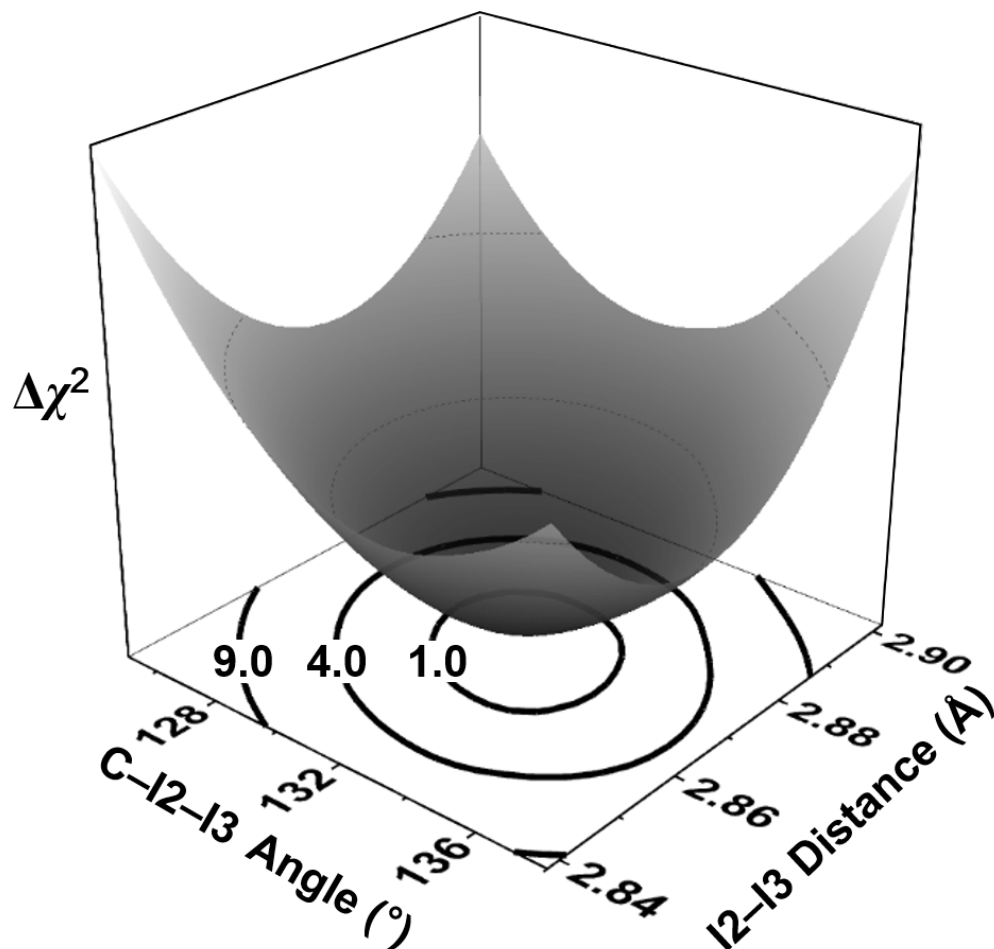


Figure S4. Three-dimensional surface and contours showing the chi-square difference ($\Delta\chi^2 = \chi^2 - \chi^2_{\min}$) as a function of $\theta_{\text{C-I-I}}$ and $d_{\text{I-I}}$ of *iso*-CHI₂-I at 100 ps. $\theta_{\text{C-I-I}}$ is varied from 105.0° to 145.0° and $d_{\text{I-I}}$ is varied from 2.220 Å to 3.820 Å with all other parameters fixed to their optimum value. The boundaries enclosing $\Delta\chi^2 = 1, 4$ and 9 , which correspond to the likelihood distribution of 68.3 %, 95 %, and 99.7 %, respectively, are indicated on the contour plot. The MINOS method in the MINUIT package estimates the error of the parameter at the likelihood boundary of 68.3 %. The optimized values of $\theta_{\text{C-I-I}}$ and $d_{\text{I-I}}$ are $133.6 \pm 2.1^\circ$ and $2.870 \pm 0.012 \text{ \AA}$, respectively, for the 100 ps structure.

SI Tables

Table S1. Optimized XYZ coordinates of the chemical species involved in the CHI₃ photolysis

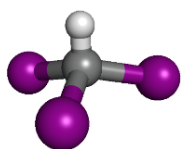
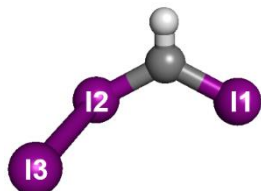
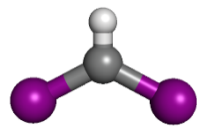

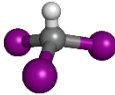
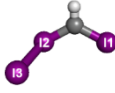
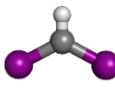

Species	Atom	X	Y	Z
	C	0.000000	0.000000	0.557566
	H	0.000000	0.000000	1.638617
	I	0.000000	2.046499	-0.031346
	I	1.772320	-1.023249	-0.031346
	I	-1.772320	-1.023249	-0.031346
	C	1.427861	0.662534	0.797652
	H	1.502056	0.799549	1.865496
	I1	2.724095	-0.659146	-0.057385
	I2	-0.247843	1.316186	-0.085631
	I3	-2.666237	-0.747131	0.017518
	C	-0.000755	0.890211	0.000000
	H	0.084591	1.964473	0.000000
	I	-0.000755	-0.068922	1.799692
	I	-0.000755	-0.068922	-1.799692
		I	0.000000	0.000000
I		0.000000	0.000000	-1.331190

Table S2. Comparison of the DFT optimized structures of the chemical species involved in CHI_3 photolysis

Species	Parameter	B3LYP/ 6- 311G**	B3LYP/ Sadlej PVTZ	B3LYP/ dhf- TZVPP +AVTZ	APFD/d hf- TZVPP +AVTZ	M06- 2X/dhf- TZVPP +AVTZ	MN12- SX/dhf- TZVPP +AVTZ	PBE0/d hf- TZVPP +AVTZ	ω B97X /6- 311G**	ω B97X /dhf- TZVPP +AVTZ	Expt. ^a
	C-I	2.181 Å	2.169 Å	2.161 Å	2.142 Å	2.134 Å	2.133 Å	2.134 Å	2.149 Å	2.130 Å	2.132 Å (± 0.010)
	I-I	3.641 Å	3.621 Å	3.603 Å	3.567 Å	3.551 Å	3.549 Å	3.553 Å	3.581 Å	3.545 Å	3.550 Å (± 0.017)
	H-C-I	105.5°	105.5°	105.7°	105.9°	106.1°	106.2°	106.0°	105.8°	106.1°	106.1° [Fixed]
	I-C-I	113.2°	113.2°	113.0°	112.8°	112.6°	112.6°	112.7°	112.9°	112.7°	112.7° [Fixed]
	C-I1	2.074 Å	2.066 Å	2.062 Å	2.142 Å	2.047 Å	2.038 Å	2.044 Å	2.056 Å	2.039 Å	2.039 Å [Fixed]
	C-I2	2.021 Å	2.006 Å	2.008 Å	1.990 Å	2.006 Å	1.977 Å	1.989 Å	2.016 Å	2.004 Å	2.004 Å [Fixed]
	I1-I3	5.934 Å	5.865 Å	5.830 Å	5.621 Å	5.535 Å	5.724 Å	5.645 Å	5.480 Å	5.392 Å	5.708 Å (± 0.025)
	I2-I3	3.163 Å	3.142 Å	3.087 Å	3.022 Å	3.127 Å	3.038 Å	3.026 Å	3.221 Å	3.181 Å	2.922 Å (± 0.004)
	C-I2-I3	130.2°	128.9°	130.4°	126.3°	120.4°	130.4°	127.0°	114.5°	114.2°	133.9° (± 0.8)
	C-I	2.082 Å	2.068 Å	2.067 Å	2.049 Å	2.049 Å	2.048 Å	2.044 Å	2.055 Å	2.039 Å	2.042 Å (± 0.010)
	I-I	3.677 Å	3.663 Å	3.642 Å	3.610 Å	3.593 Å	3.590 Å	3.599 Å	3.633 Å	3.599 Å	3.605 Å (± 0.017)
	I-C-I	124.0°	124.7°	123.5°	123.5°	122.6°	122.5°	123.4°	124.3°	123.9°	123.9° [Fixed]
	I-C-H	116.2°	116.9°	116.1°	116.9°	116.7°	115.8°	116.9°	117.9°	118.0°	118.0° [Fixed]
	I-I	2.738 Å	2.721 Å	2.703 Å	2.668 Å	2.659 Å	2.662 Å	2.664 Å	2.695 Å	2.662 Å	2.662 Å (± 0.071)

^aExperimental structures determined by global-fit analysis with errors shown in the parenthesis.

The parameters fixed at the values obtained from the ω B97X/dhf-TZVPP+AVTZ are also indicated.

Table S3. Optimized structural parameters calculated at each time delay

Time delays	d_{I-I} (Å)	θ_{C-I-I} (°)
100 ps	2.870 (\pm 0.012)	133.6 (\pm 2.1)
300 ps	2.878 (\pm 0.010)	135.0 (\pm 2.1)
1 ns	2.950 (\pm 0.008)	130.0 (\pm 1.7)
3 ns	2.916 (\pm 0.078)	134.3 (\pm 4.1)
10 ns	2.966 (\pm 0.009)	134.3 (\pm 1.5)
30 ns	2.893 (\pm 0.012)	137.1 (\pm 3.0)
300 ns	3.044 (\pm 0.043)	137.7 (\pm 4.2)
1 μ s	2.894 (\pm 0.062)	140.7 (\pm 4.3)
Average ^a	2.922 (\pm 0.004)	133.9 (\pm 0.8)

^aWeighted average

SI References

- (1) Ihee, H. Visualizing Solution-Phase Reaction Dynamics with Time-Resolved X-ray Liquidography. *Acc. Chem. Res.* **2009**, *42*, 356-366.
- (2) Ihee, H.; Wulff, M.; Kim, J.; Adachi, S.-i. Ultrafast X-ray Scattering: Structural Dynamics from Diatomic to Protein Molecules. *Int. Rev. Phys. Chem.* **2010**, *29*, 453-520.
- (3) Chai, J. D.; Head-Gordon, M. Systematic Optimization of Long-Range Corrected Hybrid Density Functionals. *J. Chem. Phys.* **2008**, *128*.
- (4) Frisch, M. J.; Trucks, G. W.; Schlegel, H. B.; Scuseria, G. E.; Robb, M. A.; Cheeseman, J. R.; Scalmani, G.; Barone, V.; Mennucci, B.; Petersson, G. A.; Nakatsuji, H.; Caricato, M.; Li, X.; Hratchian, H. P.; Izmaylov, A. F.; Bloino, J.; Zheng, G.; Sonnenberg, J. L.; Hada, M.; Ehara, M.; Toyota, K.; Fukuda, R.; Hasegawa, J.; Ishida, M.; Nakajima, T.; Honda, Y.; Kitao, O.; Nakai, H.; Vreven, T.; Montgomery, J. A.; Peralta, J. E.; Ogliaro, F.; Bearpark, M.; Heyd, J. J.; Brothers, E.; Kudin, K. N.; Staroverov, V. N.; Kobayashi, R.; Normand, J.; Raghavachari, K.; Rendell, A.; Burant, J. C.; Iyengar, S. S.; Tomasi, J.; Cossi, M.; Rega, N.; Millam, J. M.; Klene, M.; Knox, J. E.; Cross, J. B.; Bakken, V.; Adamo, C.; Jaramillo, J.; Gomperts, R.; Stratmann, R. E.; Yazyev, O.; Austin, A. J.; Cammi, R.; Pomelli, C.; Ochterski, J. W.; Martin, R. L.; Morokuma, K.; Zakrzewski, V. G.; Voth, G. A.; Salvador, P.; Dannenberg, J. J.; Dapprich, S.; Daniels, A. D.; Farkas, Foresman, J. B.; Ortiz, J. V.; Cioslowski, J.; Fox, D. J., Gaussian 09, Revision B.01. Wallingford CT, 2009.
- (5) Kim, J.; Kim, T. K.; Ihee, H. Density Functional and Spin-Orbit Ab Initio Study of CF₃Br: Molecular Properties and Electronic Curve Crossing. *J. Phys. Chem. A* **2011**, *115*, 1264-1271.
- (6) Weigend, F.; Baldes, A. Segmented Contracted Basis Sets for One- and Two-Component Dirac-Fock Effective Core Potentials. *J. Chem. Phys.* **2010**, *133*, 174102.
- (7) Refson, K. Moldy: a Portable Molecular Dynamics Simulation Program for Serial and Parallel Computers. *Comput. Phys. Commun.* **2000**, *126*, 310-329.
- (8) Ihee, H.; Lorenc, M.; Kim, T. K.; Kong, Q. Y.; Cammarata, M.; Lee, J. H.; Bratos, S.; Wulff, M. Ultrafast X-ray Diffraction of Transient Molecular Structures in Solution. *Science* **2005**, *309*, 1223-1227.
- (9) Kim, T. K.; Lorenc, M.; Lee, J. H.; Russo, M.; Kim, J.; Cammarata, M.; Kong, Q. Y.; Noel, S.; Plech, A.; Wulff, M.; Ihee, H. Spatiotemporal Reaction Kinetics of an Ultrafast Photoreaction Pathway Visualized by Time-Resolved Liquid X-ray Diffraction. *Proc. Natl. Acad. Sci. USA* **2006**, *103*, 9410-9415.
- (10) James, F.; Roos, M. Minuit - System for Function Minimization and Analysis of Parameter Errors and Correlations. *Comput. Phys. Commun.* **1975**, *10*, 343-367.
- (11) Haldrup, K.; Christensen, M.; Cammarata, M.; Kong, Q. Y.; Wulff, M.; Mariager, S. O.; Bechgaard, K.; Feidenhans'l, R.; Harrit, N.; Nielsen, M. M. Structural Tracking of a Bimolecular Reaction in Solution by Time-Resolved X-ray Scattering. *Angew. Chem. Int. Ed.* **2009**, *48*, 4180-4184.
- (12) Preston, T. J.; Shalowski, M. A.; Crim, F. F. Probing the Photoisomerization of CHBr₃ and CHI₃ in Solution with Transient Vibrational and Electronic Spectroscopy. *J. Phys. Chem. A* **2013**, *117*, 2899-2907.
- (13) Zheng, X. M.; Phillips, D. L. Solvation can Open the Photoisomerization Pathway for the Direct Photodissociation Reaction of Diiodomethane: Transient Resonance Raman Observation of the Isodiiodomethane Photoproduct from Ultraviolet Excitation of Diiodomethane in the Solution Phase. *J. Phys. Chem. A* **2000**, *104*, 6880-6886.

- (14) Phillips, D. L.; Fang, W. H. Density Functional Theory Investigation of the Reactions of Isodihalomethanes (CH₂X-X where X = Cl, Br, or I) with Ethylene: Substituent Effects on the Carbenoid Behavior of the CH₂X-X Species. *J. Org. Chem.* **2001**, *66*, 5890-5896.
- (15) Vincent, J.; Andersson, M.; Eklund, M.; Wöhri, A. B.; Odelius, M.; Malmerberg, E.; Kong, Q.; Wulff, M.; Neutze, R.; Davidsson, J. Solvent Dependent Structural Perturbations of Chemical Reaction Intermediates Visualized by Time-Resolved X-ray Diffraction. *J. Chem. Phys.* **2009**, *130*, 154502.